Submillimeter Astrophysics and Technology: A Symposium Honoring Thomas G. Phillips
ASP Conference Series, Vol. 417, © 2009
D. C. Lis, J. E. Vaillancourt, P. F. Goldsmith, T. A. Bell,
N. Z. Scoville, and J. Zmuidzinas, eds.

Sunyaev-Zeldovich Effect Studies of Galaxy Clusters with Bolocam (and Future Instrumentation)

Sunil Golwala

Division of Physics, Mathematics, and Astronomy, Mail Code 367-17, California Institute of Technology, Pasadena, CA 91125

Silvia Ameglio, Elena Pierpaoli

Department of Physics and Astronomy, University of Southern California, Los Angeles, CA 90089

Jack Sayers

Jet Propulsion Laboratory, California Institute of Technology, Mail Stop 169-506, 4800 Oak Grove Drive, Pasadena, CA 91109

Abstract. Galaxy clusters are excellent laboratories for studying the astrophysics of gravitational collapse and the non-self-similar processes that can affect it. A number of different techniques allow us to study the distribution of the consituents of galaxy clusters. The thermal Sunyaev-Zeldovich effect measures the line-of-sight integral of the the pressure in the ICM plasma. Comparison to and combination with other probes enables a variety of studies of the ICM and of clusters: scaling relations, radial profiles, tests of hydrostatic equilibrium, etc. We report on the status of our program to image clusters in the thermal Sunyaev-Zeldovich effect at 150 GHz using Bolocam and perform such tests. We also describe the upcoming MKIDCam long-wavelength multi-color facility camera for the CSO, which will provide new capabilities in thermal Sunyaev-Zeldovich effect imaging. We comment on the role Tom Phillips and the CSO have played in facilitating the development of mm-wave SZ observations.

1 Scientific Motivation

Galaxy clusters are the largest collapsed objects in the universe. They provide laboratories for studying the astrophysics of gravitational collapse, including the effects of radiative cooling, star formation, turbulence, magnetic field support, and cosmic ray pressure. To better understand such processes, improved measurements of the thermodynamic state of the intra-cluster medium (ICM) are needed, especially at large radii (e.g., Nagai et al. 2007; George et al. 2009). Additionally, the normalization and evolution of the cluster number density is sensitive to the growth of structure and the volume of space. Therefore, cluster samples with well understood masses, redshifts, and selection functions can yield precise constraints on the properties of dark matter, dark energy, and the amplitude of density fluctuations (e.g., Holder et al. 2001). However, to obtain such constraints, we need to study clusters in detail to quantify the bias and scatter in the relations between observables and cluster mass.

1.1 Current Observations

X-ray observations have been used to study the ICM (e.g., Vikhlinin et al. 2005; George et al. 2009). Although these studies have produced detailed profiles of the ICM gas properties in the inner regions of the clusters, it is difficult to study the outer regions with X-ray data alone because of the density-squared dependence of the X-ray brightness, $S_X \propto n_e^2 T_e^{1/2}/(1+z)^4$. This point is especially true of attempts to measure the X-ray temperature spectroscopically, where even more photons are needed. Moreover, at r_{vir}, the virial radius of the cluster, the Cosmic X-ray Background (CXB) is more than ten times brighter than a typical cluster (Vikhlinin et al. 2005). *Suzaku*, because of its extremely low and stable particle background due to its location within the Earth's magnetopause, is in general the only X-ray facility capable of subtracting the background with the required precision to measure temperature spectra past $0.5\,r_{vir}$. To date, measurements of temperature profiles out to r_{vir} have only been determined for a handful of clusters (Solovyeva et al. 2007; Reiprich et al. 2008; George et al. 2009).

An alternative method to extend the temperature profiles to larger radii, along with improving the accuracy to which they are determined, is to combine the X-ray data with thermal Sunyaev-Zel'dovich (tSZ) effect observations (e.g., Yoshikawa & Suto 1999; Lee & Suto 2004; Ameglio et al. 2007; Puchwein & Bartelmann 2007; Nord et al. 2009). With this technique, the temperature profile can be determined without an X-ray spectral measurement due to the different density and temperature dependence of the tSZ surface brightness (Sunyaev & Zeldovich 1972), $S_{SZ} \propto n_e T_e$. Several joint X-ray/tSZ analyses have been performed (e.g., Benson et al. 2006; LaRoque et al. 2006; Bonamente et al. 2008), but only recently have tSZ data been used in measuring temperature profiles to a significant fraction of r_{vir} (Mroczkowski et al. 2008; Nord et al. 2009). In the first model-independent joint deprojection, Nord et al. combined *XMM-Newton* X-ray data with APEX-SZ tSZ data for the cluster Abell 2163 (Nord et al. 2009). Compared to using the X-ray data alone, they were able to reduce the temperature measurement uncertainty by a factor of 2 to 3 and extend the temperature profile by a factor of $\simeq 2$ to near r_{vir}.

1.2 Cluster Astrophysics

In general, clusters are well-behaved objects, and most of their properties can be explained by simple models of gravitational collapse. Excluding the core, this is especially true in the inner regions of the cluster where X-ray observations are most sensitive (Vikhlinin et al. 2005). Typically, this data can be described by the isothermal β model (Cavaliere & Fusco-Femiano 1976), and deviations only show up at reasonable fractions of r_{500} ($\sim 0.5\,r_{vir}$) (Vikhlinin et al. 2005; Mroczkowski et al. 2008).[1] However, observational data at larger radii clearly favor models that include more complicated processes such as radiative cooling and star formation (Kravtsov et al. 2006; Nagai et al. 2007). Therefore, it is important to constrain the properties of the ICM at large radii ($> 0.25\ r_{vir}$) in order to test for these and other non-self-similar effects, and to constrain their size and nature to thereby obtain a more complete understanding of cluster for-

[1] r_{500} is the radius at which the density is 500 times the background density.

mation and astrophysics. For example, simulations and observations show that the temperature of the ICM drops beyond $\simeq 0.3\, r_{vir}$, indicating that conduction is not important on the time scales of cluster formation (Roncarelli et al. 2006; Nagai et al. 2007). The temperature peak inside r_{500} provides clues for studying processes such as shock heating during infall (George et al. 2009). Additionally, measurements of the ICM near the cluster edge provide information about accretion of matter onto the cluster; recent *Suzaku* observations near r_{vir} provide hints that the infalling gas may not be dynamically stable (George et al. 2009). Constraining the baryon fraction in the ICM, and verifying that it approaches the universal value in the cluster outskirts, will also provide vital information about cluster formation. Observations are now starting to confirm this (George et al. 2009; Nord et al. 2009).

1.3 Clusters and Cosmology

Clusters are the largest, and most recent, objects to form in the universe. They provide a tool for understanding the growth of structure at late times when cosmic acceleration from dark energy is important. The number density of clusters above a given mass as a function of redshift is sensitive to the properties of dark matter and dark energy $(\Omega_m, \Omega_\lambda, w)$ and the amplitude of density fluctuations (σ_8) (Haiman et al. 2001; Holder et al. 2000, 2001). Additionally, constraints on dark energy obtained from cluster surveys are highly complementary to those obtained from supernovae. Recently, Vikhlinin et al. used a sample of 37 high redshift clusters to constrain w to $\simeq 5\%$, an improvement by a factor of ~ 2 compared to constraints obtained without cluster data (Vikhlinin et al. 2009b). The cluster masses were determined using the quantity $Y_X = T_X \times M_{gas}$,[2] which has been shown in simulations to be a low-scatter ($< 10\%$) cluster mass estimator (Kravtsov et al. 2006; Vikhlinin et al. 2009a).

Although the $Y_X - M_{tot}$ relation has been tested extensively in simulations, it has only been verified observationally in low-z clusters. Therefore, further studies of this relation, especially at high-z, are useful. M_{tot} can be determined independently under the assumption of hydrostatic equilibrium, but accurate temperature profiles to large radii are required; these profiles can be obtained for high-z clusters by combining X-ray and tSZ data (Ameglio et al. 2007). Additionally, the joint X-ray/tSZ temperature is found independently of the X-ray spectral temperature, allowing for tests of systematics in determining T_X from X-ray spectra alone. Techniques that directly estimate cluster mass, such as gravitational lensing and member galaxy kinematics, are also useful, though they tend to be less precise at higher redshifts ($z > 0.5$).

Y_{SZ}, the integrated tSZ flux of the cluster, is also thought to trace M_{tot} within 10% based on simulations (Kravtsov et al. 2006). Currently, the Atacama Cosmology Telescope (Kosowsky et al. 2006) and South Pole Telescope (Ruhl et al. 2004) are undertaking surveys of hundreds to thousands of square degrees to detect clusters blindly via the tSZ effect. Their motivation is that, under the assumption of self-similar collapse, the cluster tSZ signal integrated over the cluster face is expected to be an excellent mass proxy: a flux-limited tSZ survey is, to a factor of 2, a mass-limited survey (Barbosa et al. 1996; Holder

[2] T_X is the flux-weighted mean X-ray spectral temperature between $0.15\, r_{500}$ and r_{500}.

et al. 2000). Thus, measurement of cluster abundance as a function of redshift using clusters selected via the tSZ effect would have a much milder redshift-dependent selection function than optical or X-ray surveys, thereby promising precise constraints on cosmological parameters, in particular Ω_m, Ω_Λ, and the equation of state parameter w (Haiman et al. 2001; Holder et al. 2001). It remains necessary to test the $Y_{SZ} - M_{tot}$ relation in a fully empirical manner and characterize the deviations from ideal behavior in order to obtain precise constraints on cosmological parameters (Majumdar & Mohr 2003; Hu 2003; Lima & Hu 2004; Majumdar & Mohr 2004). The only tests to date have been of the relations between Y_{SZ} and other quantities all derived from isothermal β-model fits to tSZ and X-ray data (Bonamente et al. 2008). Clearly, such work does not yet test whether the empirical Y_{SZ}, derived from tSZ data alone without a β-model fit to a resolved cluster, is a good mass proxy.

2 Bolocam Thermal Sunyaev-Zeldovich Effect Imaging Program

To study the above issues, we are planning to undertake a joint deprojection analysis of a sample of clusters for which we have obtained tSZ data using the Bolocam 150 GHz camera on the Caltech Submillimeter Observatory and for which there is public archival X-ray data from *XMM-Newton* and *Chandra*. Tests of the relations between various mass proxies will also be possible. Furthermore, we are expanding our sample, initially using Bolocam and later with the new CSO/MKIDCam multicolor mm-wave camera.

2.1 Deprojection Analysis: Method, Expected Precision, and Results

The technique we plan to use, developed by Ameglio et al. (2007), models the cluster as a set of spherically symmetric concentric shells. One fits for the gas density and temperature in each shell by maximizing the joint tSZ/X-ray image likelihood. A term is included in the likelihood to minimize the sum of the squares of the second derivatives of the density and temperature to prevent non-physical oscillations in the reconstruction; X-ray substructure is excised to render the data consistent with this constraint. A Markov Chain Monte Carlo approach is employed for maximization and to evaluate uncertainties. Systematic effects due to lack of spherical symmetry have been assessed by performing the analysis on three different lines of sight along the principal axes of simulated clusters. An ellipsoidal structure for the cluster can be used to mitigate the effect of this assumption. In contrast to most prior work studying radial profiles (e.g., Vikhlinin et al. 2005; Nagai et al. 2007; Mroczkowski et al. 2008), this deprojection analysis has the advantage of being model-independent.

In Figure 1, this analysis has been applied to simulated X-ray and tSZ data sets of sensitivity comparable to ours. The density profile is recovered with high precision, while the temperature profile is more finely binned and has uncertainties smaller than X-ray spectroscopic data (see Fig. 1 for further detail). For high-redshift clusters, the deprojected temperature profile will reach to larger radius than is possible with X-ray spectroscopic temperatures.

Temperature profiles of such precision would enable tests of the type discussed in Section 1.2. The direct image-space reconstruction of the density and

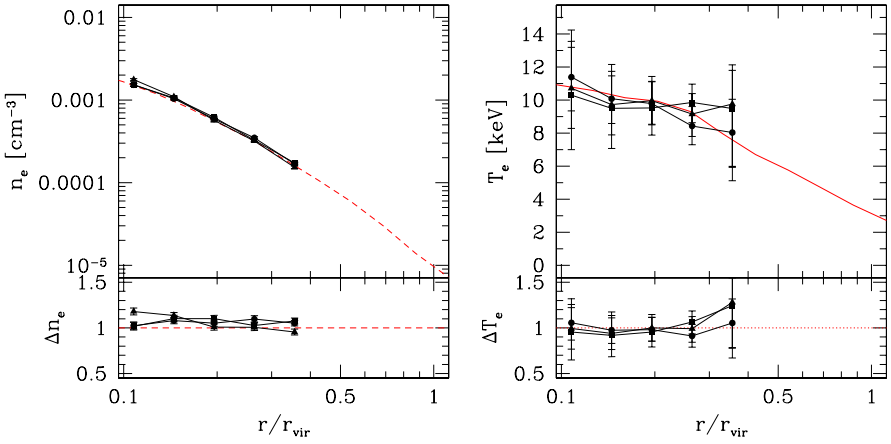

Figure 1. Expected reconstructed density and temperature profiles for a simulated $z = 0.6$ cluster based on X-ray and tSZ sensitivities comparable to available data (*Chandra*/*XMM-Newton* and Bolocam). The cluster parameters are: $r_{vir} = 3.3\,\mathrm{Mpc}$, $M_{vir} = 2 \times 10^{15}\,\mathrm{M}_{\odot}$, mass-weighted $T_e = 9.3\,\mathrm{keV}$. In angular units, $r_{vir} = 8.2'$; our current Bolocam reduction is trustworthy to a radius of about $2.5'$, the range over which we have plotted the data. We believe it can be extended to about $5'$ (see Sect. 2.4). The three sets of points with error bars in the plots are the reconstructions of density and temperature along the three different lines of sight, while the dashed line is the average profile of the input simulated cluster. Figure provided by S. Ameglio.

temperature profiles is uninfluenced by model assumptions, and thus direct tests of those assumptions can be made. The derived density and temperature profiles can be used to distinguish between models and simulations that do or do not include non-self-similar phenomena (e.g., radiative cooling). Assuming hydrostatic equilibrium, one can reconstruct the cluster mass and thus the cluster baryon fraction as a function of radius and thereby test for missing baryons and study on what scales, if any, the cluster baryon fraction matches the universal value. With the addition of gravitational lensing or galaxy kinematic data, the hydrostatic equilibrium assumption can be abandoned, too. Such an analysis of a resolved cluster has only been done in one case to date, that of the low-redshift cluster A2163 (Nord et al. 2009). Studies of this type over a wide range of redshifts would check for evolution in the behavior of the ICM radial profile and the baryon fraction, as might be expected due to evolution in merger rates, star formation rates, and the strength of magnetic field and cosmic ray pressure.

2.2 Testing Relations between Mass Proxies

Tests to date of scaling relations between X-ray and tSZ observables have proceeded through β and generalized models (Bonamente et al. 2008; Mroczkowski et al. 2008). Tests of the relation between the observables and total cluster mass have made similar assumptions. In contrast, our analysis will yield model-independent results, relying only on the physical assumption that the electrons that emit X-rays are the same ones that scatter the CMB via the tSZ effect. Deprojected temperature profiles will provide new estimates of traditionally X-

ray-only quantities, like T_X and M_{gas}. To obtain total mass estimates, we will assume hydrostatic equilibrium to obtain the underlying dark matter profile (Ameglio et al. 2009). This approach, while not fully empirical, is not model-dependent. Mass estimates based on gravitational lensing and velocity dispersion analyses are available for a subset of our clusters. Collaborator T. Szabo has developed mass estimators from peculiar velocities in SDSS data and has in hand the largest existing SDSS-based cluster catalog, extending to $z = 0.6$–0.7.

2.3 Cluster Sample

Careful study of the physical scales accessible in Bolocam observations — roughly $1'$ to $5'$ (see Sect. 2.4) — along with comparison to other tSZ programs has led us to conclude that Bolocam is optimal for relatively high z clusters, $z = 0.4$ to 1. This range is appealing for a number of scientific reasons, too. It is the regime in which the number of clusters per redshift bin in large area surveys both peaks and begins to show appreciable dependence on cosmological parameters (Ruhl et al. 2004), so it is the range in which statistical precision will be best and thus quantifying systematic uncertainties in mass estimation is most important. This redshift range contains the MAssive Cluster Survey (MACS) (Ebeling et al. 2001) high-z sample, which is a complete sample of 12 clusters at $z > 0.5$ with a wide range of followup data (Ebeling et al. 2007). Finally, and most critical for studies of cluster thermodynamics, X-ray data do not degrade very quickly due to cosmological dimming in this range of z because: 1) the $(1+z)^{-4}$ factor is relatively mild for $z < 1$; and 2) the increase in angular diameter distance with z implies that a particular bin in physical radius becomes smaller in angle as z increases, resulting in decreased instrumental background per radial bin, which significantly compensates for cosmological dimming. We expect a degradation of only a factor of about 1.6 in X-ray signal-to-noise per *physical* radius bin between $z = 0.2$ and $z = 1$, implying our deprojection analysis will not be significantly adversely affected.

Currently, our sample has 17 completed clusters, of which 10 have $z > 0.4$ and 12 have $z > 0.3$. Two more clusters are partially complete, one of them with $z > 0.4$. The tSZ data have been fully reduced for 8 of the completed clusters, while quick-look analyses give approximate depths for the remainder. We have analyzed public Chandra data for 8 clusters in our sample. The X-ray analysis follows the standard methodology used in (e.g., Vikhlinin et al. 1998, 2005; Benson et al. 2006; Mroczkowski et al. 2008; Markevitch et al. 2003).

Our tSZ data set is among the largest samples of clusters with mm-wave tSZ imaging to date. It has significant overlap with the early BIMA-OVRO 30 GHz interferometric sample (Bonamente et al. 2008), but the very different systematics and spatial filters inherent in imaging and interferometric data make it important and interesting to have data sets of both types. SZA has obtained a sample of approximately 70 clusters at 30 GHz (Marrone, private comm.), but has focused on lower redshifts, $z \sim 0.2$ to 0.3, and has angular resolution of $2'$. The samples are thus quite complementary. We are actively expanding our sample at the rate of 5–7 clusters a semester.

We also aim to maximize overlap with complementary observations with other instruments. The CBI2, AMI, and AMiBA interferometers have coarser angular resolution and sensitivity to larger spatial scales than Bolocam. AzTEC

and SCUBA2 have better angular resolution and are more sensitive to submillimeter galaxies, which may contaminate our cluster maps at a low level. We have already coordinated with CBI2 and AzTEC by sharing source lists.

2.4 Bolocam tSZ Data Set

Figure 2 shows a map of the cluster MS0451 ($z = 0.55$) that is representative of our data. It was obtained in 15 on-source hours, requiring roughly 3 nights.

MS0451 is similar to the simulated cluster shown in Figure 1: the BIMA-OVRO-*Chandra* analysis (Benson et al. 2006; Bonamente et al. 2008) gives similar T_e (9.9 keV). From this, we may conclude $r_{2500} \approx 525\,\mathrm{kpc} \approx 0.15\,r_{vir} \approx 1.3'$, $r_{500} \approx 1.7\,\mathrm{Mpc} \approx 0.5\,r_{vir} \approx 4.3'$, and $r_{vir} \approx 3.3\,\mathrm{Mpc} \approx 8.6'$. Therefore, our map demonstrates sensitivity on the angular scales of interest (Sect. 2.1).

To acquire the data, the telescope is scanned in a Lissajous pattern (incommensurate sine wave drives in RA and declination), which is approximately optimal for a science field of this size in the presence of atmospheric optical loading fluctuations (sky noise) as long as scan-synchronous artifacts due to telescope motion are negligible (Sayers et al. 2008, 2009; Kovacs 2008). The scan pattern has periods of 5 to 10 seconds in each direction and moves the telescope boresight over a $8' \times 8'$ square, which, when integrated over the entire focal plane, yields a tapered coverage pattern for which the integration time at the edges of a $8' \times 8'$ square centered on the cluster is only two times less than at the center ($\sqrt{2}$ in noise); see Figure 2. A single observation is 10 minutes long.

Scan-synchronous signals and sky noise are removed as follows. First, scan-synchronous signals appearing at the Lissajous scan frequency and harmonics are filtered from the timestreams, resulting in a high-pass filter at roughly 0.1 Hz, notching between 0.1 and 0.5 Hz, and no filtering above 0.5 Hz. Next, detectors more than $2'$ from the cluster center are used to construct a sky noise template that depends quadratically on detector position; the coefficients of the quadratic are allowed to change with the time-dependent spatial shape of the atmospheric emission. This template is regressed out of every detector's timestream using a single regression coefficient per detector over the entire observation.

Maps are made by binning the data into map pixels with weighting by the given detector's point-source sensitivity derived from its timestream noise power spectral density for the observation. Observations of bright point-like sources, including Uranus and Neptune, are used to measure the location of the detectors on the sky, correct for telescope pointing offsets as a function of time, measure the beam shape of each detector, and perform relative and absolute flux calibration as a function of atmospheric opacity. Residual pointing uncertainties are at the $5''$ level (negligible compared to the $1'$ FWHM beam) and the flux calibration uncertainty is dominated by the model uncertainty in the Mars model against which the flux of Uranus and Neptune are referenced (Sayers et al. 2009).

The complex transfer function of the observing and data reduction is measured by inserting model clusters into the data timestreams for that cluster, repeating the entire data reduction and mapping process, and then differencing the model-added map from the map made with no model added. We verified this technique during our tSZ survey analysis (Sayers et al. 2009). Figure 3 shows an input and processed model cluster along with the derived Fourier-space transfer function. Measuring the transfer function in Fourier space is an approximation

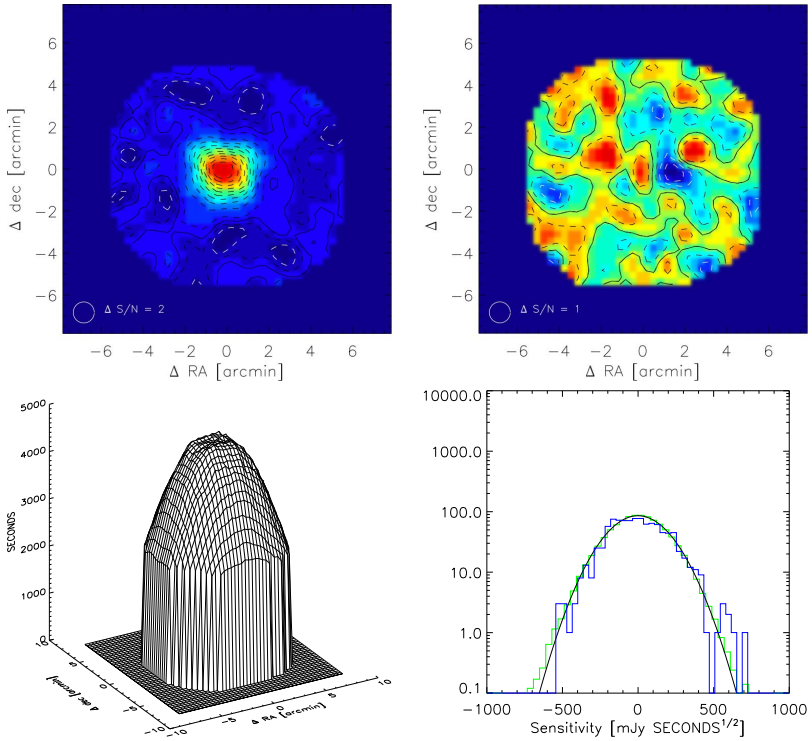

Figure 2. Bolocam tSZ observations. **Top left**: MS0451 beam-smoothed signal-to-noise map, contours are $\Delta S/N = 2$. The unsmoothed beam FWHM ($1'$) is shown. **Top right**: Subaru/XMM Deep Survey (SDS1) blank field beam-smoothed signal-to noise map (contours are $\Delta S/N = 1$), showing no apparent artifacts. **Bottom left**: Coverage map for MS0451 observations in seconds per $20'' \times 20''$ pixel. **Bottom right**: Histogram of pixel value $\times$ $\sqrt{\text{integration time}}$ in an ensemble of 100 MS0451 jackknifes (green/light), in SDS1 blank field (blue/dark), with Gaussian fit (black). Both histograms are quite Gaussian, indicating, respectively, well-behaved noise properties and an absence of scan-synchronous artifacts.

because the reduction is not a translation-invariant process, but it is useful for characterizing the reduction's spatial dynamic range.

The noise properties of the data are evaluated as follows. First, to demonstrate that the observing and data reduction result in no appreciable artifacts, we map known blank fields (see Fig. 2). Next, given the success of this test, we obtain signal-free realizations of the noise by constructing jackknife maps — maps that are made in the same manner as the true cluster maps, but with -1 factors multiplying a random half of the observations. Assuming the noise is uncorrelated between any pair of ten-minute observations, this procedure preserves the noise statistics while removing the signal.[3] Given that roughly 60 to

[3] A caveat: the jackknifing procedure does not null astronomical signal contributions to off-diagonal elements of the map-space noise covariance matrix. However, we observe these to be

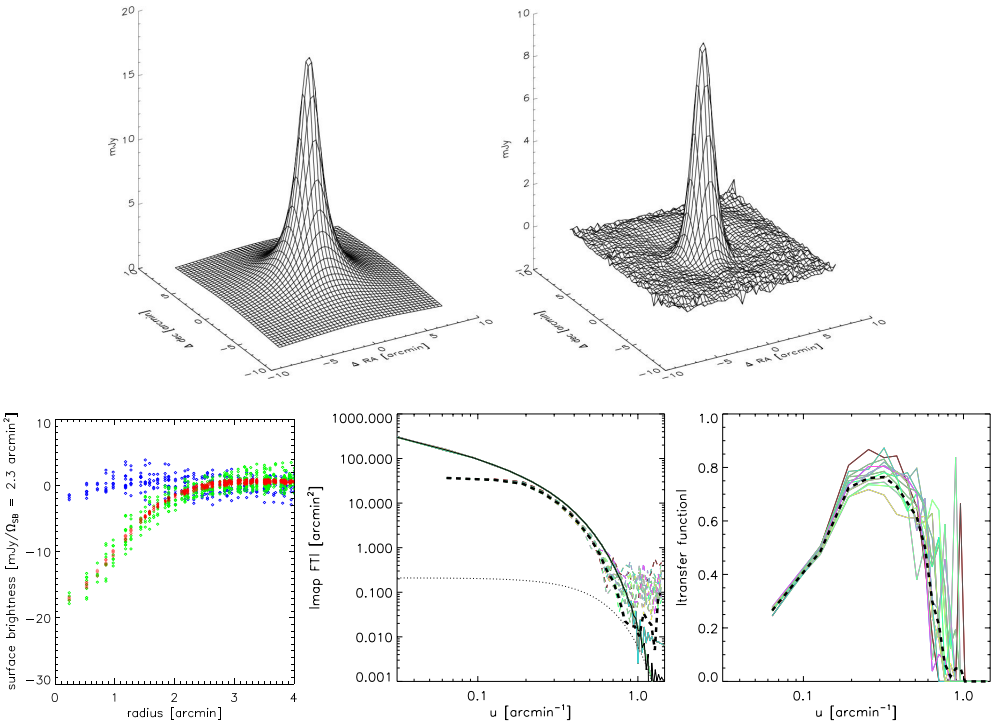

Figure 3. Transfer function of Bolocam tSZ analysis observing/analysis pipeline. **Top left**: input beam-smoothed model cluster using best-fit BIMA/OVRO/*Chandra* β model for MS0451 (Benson et al. 2006), with Comptonization $y_0 = 2.7 \times 10^{-4}$, $\beta = 0.795$, and $r_c = 36''$. (For the sake of clarity, we plot the signal as a positive flux.) **Top right**: model cluster after processing by Bolocam pipeline. **Bottom left**: radial profiles for MS0451 (green/light), SDS1 (blue/dark), and processed model cluster (red/light with tight scatter). Each point corresponds to one map pixel. The fit of the processed model cluster to observed data is quite good, including even the opposite polarity excursion at large radius. The SDS1 profile is consistent with no signal. **Bottom center**: magnitude of Fourier transform of beam-smoothed input (solid) and processed (dashed) clusters as a function of inverse wavelength. The multiple lines are taken at different azimuthal angles in Fourier space. The heavy dashed line is the average over azimuthal angles. The noise at high u occurs due to pixellization of the simulated map; this is both unimportant and can be remedied. The dotted line is the shape of the beam. **Bottom right**: magnitude of the Fourier-space transfer function, which is the ratio of the processed to input cluster model in Fourier space. The legend is as for the previous plot, and the high-u noise has the same source. The transfer function is ≈ 0.75 for scales smaller than $5'$ and it has appreciable value even at $16'$ scales, indicating that there is the prospect of recovering large-scale signal with a more sophisticated mapmaker. Also, the β-model diverges unphysically as $u \to 0$.

100 ten-minute observations are taken on a given source, the residual signal in the jackknifes is negligible and the precision of the noise estimate is limited by the number of jackknifes (typically 1000). The noise is remarkably Gaussian after correction for variations in integration time, as is shown in Figure 2. This provides precise estimates of the signal-to-noise in each map pixel. The complex scan pattern results in no significant map-space noise covariance between pixels; it is reasonable to assume the noise is uncorrelated in map space.

We thus have a mature observing and reduction pipeline with fully characterized signal transfer function and noise properties. However, computing the transfer function for a candidate cluster model is time-consuming. For the MCMC search, we will characterize the transfer function of the analysis on a grid of pre-calculated analytical models, β or Nagai (Nagai et al. 2007) profiles, interpolate the transfer function between these models, and then apply the transfer function that is "nearest" to a candidate deprojection to obtain a map that can be compared to the data. Once the MCMC has converged, we can then run the optimal deprojection and a set of deprojections in its uncertainty neighborhood through the full pipeline to check that it is indeed the best fit to the data. Errors will be calculated using the Markov Chain and simulations.

We note the current analysis is non-optimal because the reduction makes no use of the complexity of the Lissajous pattern to optimally separate astronomical signal from sky noise. We thus lose signal on scales $> 5'$, as seen in the transfer function. Clearly, though, since the transfer function does not vanish even at the $(16')^{-1}$ scale, information on these largest scales is preserved. A more sophisticated pipeline will likely recover information out to $10'$ scales.

To obtain the sensitivity estimates in Section 2.1, we did not do a full analysis using the signal transfer function. Rather, we degraded the observed noise level in our MS0451 map (0.8 mJy/1.4′ FWHM smoothed beam, or 11 $\mu\mathrm{K}_{CMB}$ and rms Comptonization $y = 4 \times 10^{-6}$) by 3.75, the ratio of the peak heights of the input (pre-beam-smoothing) and pipeline-processed MS0451-type cluster model (Fig. 3), to account for the signal loss. This is conservative, as it assumes the noise on all scales is degraded equally by the transfer function of the pipeline; Figure 3 indicates a range of scales are only mildly attenuated.

3 MKIDCam

The future prospects for a further expanded sample, with access to larger spatial scales, are good. We are constructing with collaborators at Caltech, JPL, and the University of Colorado a new four-color facility camera for the CSO with bands at 220, 275, 350, and 405 GHz *in each spatial pixel*, MKIDCam. The camera will have 600 spatial pixels over a 14′ field-of-view. It will be commissioned in mid-2010. The orthogonality of the tSZ spectrum and the atmosphere over these bands will enable *spectral* sky subtraction in each pixel, first pioneered by SuZIE (Mauskopf et al. 2000; Benson et al. 2003, 2004). Recent work confirms the expectation that the sky noise is modeled well by assuming that the rms fluctuation in precipitable water vapor (PWV) is, on average, proportional to the

---

small for all but the brightest clusters, and neglecting such covariances will result in an overestimate of the map-space noise covariance, which we note below can be neglected, regardless.

total PWV and that atmospheric brightness fluctuations at various frequencies are determined entirely by the the variation in opacity with PWV (Sayers et al. 2009), which can be determined from atmospheric models (Pardo et al. 2001a,b, 2005). Since PWV fluctuations drive the opacity variations, these will be well correlated among different observing bands. Thus, one can remove sky noise spectrally, eliminating the spatial filter imposed by sky noise removal in our current reduction and thereby providing access to larger angular scales. The only limit will be instrument $1/f$ noise. It will also yield improved instantaneous sensitivity, as residual sky noise currently limits the sensitivity of Bolocam, even at 150 GHz, and causes factors of 2 variation in instantaneous sensitivity with atmospheric conditions. Access to the high-frequency bands will also enable tests for contamination by submillimeter galaxies. MKIDCam is described in detail in (Glenn et al. 2008).

4 CCAT

CCAT tSZ imaging promises to be fruitful. The strawman long-wavelength camera, LWCam, will cover the $20'$ field-of-view of CCAT at 2.5 times finer angular resolution than CSO. Coverage from 405 GHz to 100 GHz in a single camera is feasible via further development of many of the MKIDCam technologies. Spectral sky noise will again be possible in such a camera. This will enable studies of clusters at larger radius and finer angular resolution at a site where the opacity and sky noise are roughly a factor of 2 better than at CSO.

5 Tom's Role

Perhaps surprising to those who know Tom Phillips primarily as a spectroscopist and the CSO mainly for its role in studying the ISM, Tom has been a longtime supporter of Sunyaev-Zeldovich effect work at the CSO. Andrew Lange brought the first bolometric SZ instrument, SuZIE, to the CSO in the early 1990s after a phone call with Tom. That instrument provided the first solid millimeter-wave detections of the SZ effect. It also seeded the next generation of SZ instruments — ACBAR at the South Pole and Bolocam on the CSO. The field has since blossomed, with projects like APEX-SZ, ACT, SPT, and MKIDCam. The careers of a number of those working in the SZ field started at the CSO. And we keep coming back with new instruments because of Tom's incredible openness to testing out new ideas and doing new science with the CSO.

Acknowledgments. We thank our Astro2010 Decadal Survey White Paper co-writers for fruitful interactions on cluster astrophysics. We acknowledge our Bolocam instrument collaborators — Peter Ade, James Aguirre, Jamie Bock, Samantha Edgington, Jason Glenn, Alexey Goldin, Douglas Haig, Andrew Lange, Glenn Laurent, Phil Mauskopf, Hien Nguyen, and Philippe Rossinot, with technical assistance from Minhee Yun, Anthony Turner, and Toshiro Hatake of JPL, Marty Gould of Zen Machine, Ricardo Paniagua and the Caltech PMA/-GPS Instrument Shop, Carole Tucker of Cardiff University, Ben Knowles, the day crew and staff of the CSO, and Kathy Deniston. Nicole Czakon and Matt Hollister participated in Bolocam observing. Bolocam was built and commissioned under NSF/AST-9618798, NSF/AST-0098737, NSF/AST-9980846, NSF/-

AST-0229008, and NSF/AST-0206158. The CSO is operated under NSF/AST-0540882 and NSF/AST-0838261. JS is supported by the NASA Postdoctoral Program. Partial support for SG and for observing has been provided by the Gordon and Betty Moore Foundation. EP is an NSF–ADVANCE fellow (NSF/AST0649899) and is also supported by NASA-NNX07AH59G. SA is supported by NSF/AST-0649899 and by the USC WiSE postdoctoral fellowship. MKIDCam is funded by NSF/AST-0705157, the Moore Foundation, and the CSO.

References

Ameglio, S., et al. 2007, MNRAS, 382, 397
Ameglio, S., et al. 2009, MNRAS, 394, 479
Barbosa, D., et al. 1996, A&A, 314, 13
Benson, B. A., et al. 2003, ApJ, 592, 674
Benson, B. A., et al. 2004, ApJ, 617, 829
Bonamente, M., et al. 2006, ApJ, 647, 25
Bonamente, M., et al. 2008, ApJ, 675, 106
Cavaliere, A. & Fusco-Femiano, R. 1976, A&A, 49, 137
Ebeling, H., et al. 2001, ApJ, 553, 668
Ebeling, H., et al. 2007, ApJ, 661, L33
Glenn, J., et al. 2008, in *Society of Photo-Optical Instrumentation Engineers (SPIE) Conference Series* (SPIE, Bellingham, Washington), Vol. 7020
George, M. R., et al. 2009, MNRAS, 395, 657
Haiman, Z., et al. 2001, ApJ, 553, 545
Holder, G. P., et al. 2000, ApJ, 544, 629
Holder, G., et al. 2001, ApJ, 560, L111
Hu, W. 2003, Phys. Rev. D, 67, 081304/1
Kosowsky, A. & ACT Collaboration 2006, New Astron. Rev., 50, 969
Kovács, A. 2008 in *Society of Photo-Optical Instrumentation Engineers (SPIE) Conference Series* (SPIE, Bellingham, Washington, Vol. 7020.
Kravtsov, A. V., et al. 2006, ApJ, 650, 128
LaRoque, S. J., et al. 2006, ApJ, 652, 917
Lee, J., & Suto, Y. 2004, ApJ, 601, 599.
Lima, M. & Hu, W. 2004, Phys. Rev. D, 70, 043504/1
Majumdar, S. & Mohr, J. J., 2003, ApJ, 585, 603
Majumdar, S. & Mohr, J. J. 2004, ApJ, 613, 41
Markevitch, M., et al. 2003, ApJ, 583, 70
Mauskopf, P., et al. 2000, ApJ, 538, 505
Mroczkowski, T., et al. 2009, ApJ, 694, 1034
Nagai, D., et al. 2007, ApJ, 668, 1
Nord, M., et al. 2009, astro-ph/0902.2131
Pardo, J., et al. 2001, ITAP, 49, 1683
Pardo, J., et al. 2001, J. Quant. Spectr. Radiat. Transf., 68, 419
Pardo, J., et al. 2005, J. Quant. Spectr. Radiat. Transf., 96, 537
Puchwein, E., & Bartelmann, M. 2007, A&A, 474, 745
Reiprich, T. H., et al. 2008, astro-ph/0806.2920, submitted to A&A
Roncarelli, M., et al. 2006, MNRAS, 373, 1339
Ruhl, J., et al. 2004, in *Proceedings of the SPIE, Vol. 5498: Millimeter and Submillimeter Detectors for Astronomy II*, edited by J. Zmuidzinas and W. S. Holland (SPIE, Bellingham, Washington), pp. 11–29
Sayers, J., et al. 2008, in *Society of Photo-Optical Instrumentation Engineers (SPIE) Conference Series* (SPIE, Bellingham, Washington), Vol. 7020
Sayers, J., et al. 2009, ApJ, 690, 1597

Sayers, J., et al. 2009, astro-ph/0904.3943, submitted to ApJ
Solovyeva, L., et al. 2007, A&A, 476, 63
Sunyaev, R. A. & Zeldovich, Y. B. 1972, Comm. Astr. Sp. Phys., 4, 173
Vikhlinin, A., et al. 1998, ApJ, 502, 558
Vikhlinin, A., et al. 2005, ApJ, 628, 655
Vikhlinin, A., et al. 2009, ApJ, 692, 1033
Vikhlinin, A., et al. 2009, ApJ, 692, 1060
Yoshikawa, K., & Suto, Y. 1999, ApJ, 513, 549